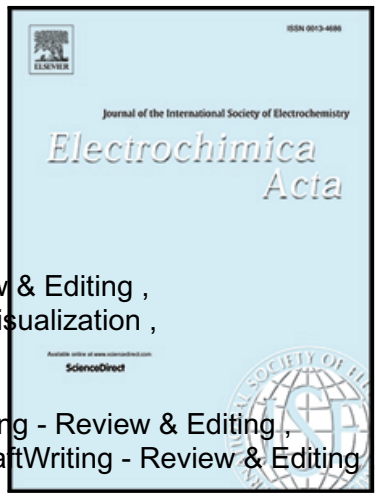

3D Titania Nanotube Array Support for Water Electrolysis Palladium Catalysts

M. Bellini MethodologyInvestigationWriting - Original DraftWriting - Review & Editing ,
E. Berretti InvestigationWriting - Original DraftWriting - Review & EditingVisualization ,
M. Innocenti , G. Magherini InvestigationVisualization ,
M.V. Pagliaro , L. Poggini ,
H.A. Miller MethodologyValidationInvestigationWriting - Original DraftWriting - Review & Editing ,
A. Lavacchi ConceptualizationMethodologyValidationWriting - Original DraftWriting - Review & Editing
F. Vizza ResourcesSupervision

PII: S0013-4686(21)00628-9
DOI: https://doi.org/10.1016/j.electacta.2021.138338
Reference: EA 138338

To appear in: *Electrochimica Acta*

Received date: 2 January 2021
Revised date: 30 March 2021
Accepted date: 3 April 2021

Please cite this article as: M. Bellini MethodologyInvestigationWriting - Original DraftWriting - Review & Editing , E. Berretti InvestigationWriting - Original DraftWriting - Review & EditingVisualization , M. Innocenti , G. Magherini InvestigationVisualization , M.V. Pagliaro , L. Poggini , H.A. Miller MethodologyValidationInvestigationWriting - Original DraftWriting - Review & Editing , A. Lavacchi ConceptualizationMethodologyValidationWriting - Original DraftWriting - Review & Editing , F. Vizza ResourcesSupervision , 3D Titania Nanotube Array Support for Water Electrolysis Palladium Catalysts, *Electrochimica Acta* (2021), doi: https://doi.org/10.1016/j.electacta.2021.138338

Highlights

- We demonstrate the growth of short nanotubes with low aspect ratio from water on titanium non-woven web.
- Magnetron sputtering is effective for the deposition of ultra-low Pd loadings on 3D TNTA.
- The ultra-low Pd loaded 3D TNTA delivers 0.3 A cm^{-2} @ 2V and 1.485 A cm^{-2} @ 2.5 as cathode in an anion exchange membrane electrolyser.
- Performance does not change significantly after 24 hrs of operation at 1 A cm^{-2} at 60 °C.

3D Titania Nanotube Array Support for Water Electrolysis Palladium Catalysts

M. Bellini[1], E. Berretti[1], M. Innocenti[2], G. Magherini[2], M. V. Pagliaro[1], L, Poggini[1], H. A. Miller[1*], A. Lavacchi[1*] and F. Vizza[1]

[1] Institute of Chemistry of Organometallic Compounds (ICCOM)—National Research Council (CNR), via Madonna del Piano 10, 50019 Sesto Fiorentino, Italy

[2] Department of Chemistry "Ugo Schiff", Università degli Studi di Firenze, via della Lastruccia 3, 50019 Sesto Fiorentino, Italy

[*]Corresponding Authors: alessandro.lavacchi@iccom.cnr.it; hamish.miller@iccom.cnr.it

Abstract

A critical step in developing deployable water electrolysis technologies is the reduction in the amount of platinum group metals (PGMs) that are the most active catalysts for hydrogen and oxygen evolution. In this paper, we demonstrate a convenient strategy to reduce the PGM loading in electrolysis by using ultra-low Pd loaded electrocatalysts supported on 3D architectures of titania (TiO_2) nanotubes. This manuscript focuses on the following aspects: 1) a comprehensive analysis of the synthesis of the TiO_2 support using water-based electrolytes; 2) the deposition of Pd catalyst to the support by either physical vapour deposition or dropcast and 3) functional characterisation of the obtained materials for hydrogen and oxygen evolution in both acidic and alkaline environments. A new strategy is developed to obtain short low aspect ratio 3D titania nanotubes arrays (TNTA) and we demonstrate that an extremely low quantity of Pd (81 µg cm^{-2}) is sufficient to obtain significant activity improvement in an Anion Exchange Membrane (AEM) water electrolyser.

Keywords

Titanium dioxide; Nanotubes; Palladium; Electrolysis; Electrocatalysis

1. Introduction

Water electrolysis is the cornerstone of the hydrogen economy paradigm [1]. It provides a convenient route to the production of hydrogen as an energy vector, relying on the use of renewable resources as primary energy supply. Despite the simplicity of the idea, its application poses severe challenges [2]. First, there is the need to make electrolysis productive enough to guarantee relevant

hydrogen output; second, is the requirement of rare and expensive platinum group metals (PGMs) electrocatalysts. PEM electrolysers are the most promising technology in terms of performance. However, they use acidic electrolytes and require a significant amount of PGMs to work (e.g. Pt, IrO_2)[3]. Well established alkaline electrolysis may avoid or limit the use of PGMs, but its H_2 productivity is low with a limited energy efficiency due to the high ohmic drop in the electrolyte [4].

Recently, the use of anion exchange membranes (AEMs) in water electrolysis has been proposed, opening up the possibility to move high-performance electrolysis from PEM technology to alkaline conditions [5,6]. The AEM environment is less aggressive compared to PEMs, and many metals and metal oxides are more stable in alkali than in acids. However, the potential of AEM electrolysis is yet to be realised. Indeed, this depends mostly on the availability of stable and high performance membranes [7,8]. It is worth mentioning that the stability of alkaline membranes is much lower compared to the acidic systems with an upper operating temperature limit of 60 °C and sensitivity to nucleophilic attack by OH species [8]. In recent years, many new membranes have been developed either by research groups or for commercial application. Many of them have received extensive functional characterisation in fuel cells [8] adopting different catalytic materials, for both the anodic and cathodic reactions.

Another factor affecting the energy efficiency of water electrolysis are the electrocatalysts used to promote the hydrogen and oxygen evolution reactions [9,10]. In PEM electrolysis, both reactions require a significant amount of PGMs to guarantee operation at current densities exceeding 1 A cm^{-2} with the capability to withstand current densities up to 6 A cm^{-2} to absorb the energy production peaks from intermittent renewable resources (e.g. [11–13]). The efficiency of the catalysts is then not only related to their chemical nature, but also to their distribution within the electrode structures. Hence, alternative catalyst layer architectures could be used to improve the durability, current and H_2 output of the electrolysis cell. To this end, this paper focuses on an original approach exploiting 3D nano-architectures of titania nanotubes (TNTA) for AEM water electrolysis. The use of this electrode support material enables the reduction in the loading of the Pd catalyst particles for both the H_2 and O_2 evolution reactions [14].

In 2014 we introduced a new class of electrocatalyst support based on the growth of anatase nanotubes on the surface of the fibres of non-woven titanium web [15]. The effectiveness of the material was shown in various applications, e.g. electrochemical reforming, alkaline direct ethanol fuel cells and photocatalysis [15–18]. The 3D Titanium Nanotube Array (TNTA) demonstrated an excellent capability to act as a support for Pd nanoparticles. Additionally, the open structure of the electrocatalyst showed excellent mass transport capabilities besides being self-standing, with a

mechanical stability exceeding that of conventional catalysts based on carbon inks. These properties are attractive for electrolysis for the following reasons: i) the material can withstand intense bubbling without the risk of losing catalyst particles ii) the use of 3D TNTA allows easy manipulation of the electrode with a powder-free assembly of the electrolytic cell and iii) the catalyst can be applied directly on the diffusion layer simplifying the architecture of the membrane electrode assembly.

However, the TNTA architectures we introduced in 2014 have some limitations. The mean nanotube length exceeds 2 μm with a 15-20 aspect ratio, which are typical values for titania nanotubes grown from organic electrolytes [15]. Such a large nanotube length to width aspect ratio has two major implications: i) it makes the fibres brittle as they contain a large fraction of oxide and ii) full exploitation of the PGM catalyst present is less likely because of the mass transport limitations inside the nanotubes. Moreover, we have observed the presence of large cracks at the edge of the fibres that may undermine the physical integrity of the TNTAs [18].

In this paper, we explore an alternative route to the synthesis of 3D TNTAs with shorter tube lengths and a lower aspect ratio. To do so, we rely on an alternative synthetic strategy based on HF water solutions, an approach that has been already proven for the growth of short nanotubes on bulk titanium surfaces [19,20] (known as first generation nanotubes). Moreover, to reduce the impact on critical raw materials, we explore a facile and scalable route for the addition of ultralow Pd loading to the nanotubes using a Physical Vapor Deposition (PVD) technique. This method has been selected as it is quick and in principle convenient to coat a solid material like the 3D TNTA based on the titanium non-woven web. Moreover, the use of PVD has already been used to deposit catalysts on high surface area supports (see e.g. [21]). We choose to explore Pd as an alternative to Pt that has been already tested in water electrolysis, particularly for the hydrogen evolution reaction and less frequently for the oxygen evolution reaction [22–25]. We confront the performance of the PVD Pd catalyst with use of Pd dropcast catalyst that has a larger Pd loading. The functionality of the proposed electrocatalyst is then explored in electrochemical cells, to determine the HER and OER specific activity. The Pd-TNTA electrode is also employed as a cathode in an AEM water electrolyser.

2. Experimental

2.1. Synthesis of TNTAs

A 1.13 cm^2 titanium non-woven web disk (Beakert, Belgium) was cleaned by a 30-minute ultrasound treatment in acetone (59 Hz, 200W). The disk was then rinsed several times with distilled water and screwed into a PTFE holder. Titanium anodization was undertaken using a two-electrode cell, in which a nickel foam sheet (10 × 10 cm size) was used as the cathode electrode, and the titanium non-woven web disk (1.13 cm^2) in the PTFE holder was the anode electrode (Figure S1). The nickel foam cathode was first cleaned in a 1M HCl (Sigma-Aldrich-Merck) aqueous solution applying ultrasound for 30 minutes (59 Hz, 200W). The distance between the cathode and anode electrodes was c.a. 1 cm and they were both immersed in a 0.5 wt% HF aqueous solution (700 g) kept under magnetic stirring (350 rpm) [26]. The anodization was carried out by applying 20V between the anode and the cathode for 20 minutes After anodization, the TNTA electrode was washed several times with distilled water, dried under air and then treated in a quartz-tube oven at 400 °C under air for 30 min [27].

2.2. Palladium deposition onto the TNTA support

Two sample types of Pd loaded TNTAs were prepared; a) a high loading series in which Pd was deposited by dropcast and b) a low loading catalyst where Pd was applied by PVD sputtering. In the high loading catalysts series, Pd was deposited onto the TNTA support by a drop-casting procedure as follows: a solution of 6.47 mg (2.12 mmol) of $Pd(acac)_2$ (Sigma-Aldrich-Merck, 99%) dissolved in 5 ml of acetone (Sigma-Aldrich-Merck, 99.5%) was deposited dropwise onto the TNTA support. The support was then dried in air at 80°C and the procedure was repeated several times until all the solution was consumed. The $Pd(acac)_2$ impregnated support was heated at 250°C for 15 minutes in an air oven to reduce the palladium salt to Pd nanoparticles. An ICP-OES analysis of the synthesized catalyst gave a palladium loading of 1.7 mg_{Pd} cm^{-2}. Palladium in the low loading catalysts was deposited by PVD in an Emitech K575x Magnetron Sputter Coater. The process parameters for the deposition were: *i)* sputtering current - 25 mA and *ii)* deposition time - 30 seconds. The cathode was a Pd disk of 99.9 wt. % purity. A 0.081 mg cm^{-2} Pd loading was determined by ICP-OES characterisation.

2.3. Three electrode electrochemical cell testing

Cyclic (CV) and linear sweep voltammetry (LSV) were performed in a standard pyrex® three-electrode cell apparatus modified in our laboratory. The reference electrode was a commercial $Ag/AgCl/KCl_{sat}$ (Princeton Applied Research), and the counter electrode was a gold gauze enclosed in a glass tube with a porous bottom. The Pd-TNTA working electrode was placed in a cylindrical PEEK holder with a round window (1.13 cm^2). A platinum wire embedded in the PEEK holder was use to electrically connect the catalyst to the potentiostat. Experiments were acquired at room temperature in 2M KOH or 0.25M $HClO_4$ aqueous solutions, prepared using Milli-Q water (18 MΩ.cm) provided with a Millipore Milli-Q^3 apparatus. Chemicals were used as purchased from Sigma-Aldrich-Merck (KOH 85% purity, $HClO_4$ 65% in water). Solutions were purged by bubbling pure N_2 for 30 minutes (OER LSVs did not require purging with N_2), and the CVs or LSVs were acquired with a Parstat 2273 potentiostat–galvanostat (Princeton Applied Research). All the potentials are reported versus the Reference Hydrogen Electrode (RHE). Cyclic voltammetry was acquired at a 20 mV s^{-1} scan rate, while linear sweep voltammetry at a 1 mV s^{-1} scan rate.

2.4. Water Electrolysis Experiments

Membrane electrode assemblies (MEAs) were prepared by sandwiching the cathode electrode, a Tokuyama A-201 anion exchange membrane (Tokuyama Corporation, Japan), and an IrO_2 based anode in a stainless steel Scribner testing cell (Scribner Corp. USA) applying a 4 Nm torque closing force. The cathode was either the 1.13 cm^2 Pd-TNTA based catalyst or a 5 cm^2 benchmark cathode based on a commercial Pt (40%) / C catalyst (Sigma. Aldrich-Merck) spread onto a carbon cloth W1S1005 (CeTech Co., Ltd.) gas diffusion layer by means of a Meyer rod (n°150), in order to obtain a 0.4 mg cm^{-2} Pt loading. The anode was prepared by mixing 30 mg of IrO_2 with 30 mg of Vulcan XC-72 and 200 mg of Nafion® ionomer (5% wt in low aliphatic alcohols). The mixture was spread onto a 5 cm^2 titanium web support, reaching the 5 mg cm^{-2} loading. The anode and the cathode were fed with 50 mL of a 2M KOH aqueous solution by a peristaltic pump (Gilson Mini Pulse) with a 1 ml min^{-1} flow rate. A Bronkhorst EL-Flow flow meter was used to quantify the H_2 produced in the cathode compartment. Electrolysis data were acquired at a cell temperature of 60°C using an ARBIN BT-2000 5A-4 channels potentiostat/galvanostat. Scan voltage curves between 0 and 2.5 V were recorded at 10 mV s^{-1} scan rate. Galvanostatic experiments were performed by applying the constant current load of 1 A cm^{-2} to the cell until the measured voltage reached the 2.5 V or after 24-hour cut-off value.

2.5. Materials characterisation

SEM, STEM and EDX sample characterisation was performed using a TESCAN Gaia 3 FIB/SEM. The microscope hosts a 30 kV Triglav electron column, and a Cobra Focused Gallium Ion Beam column. SEM images of the sample surfaces were acquired using the two in-beam Secondary Electron (SE) and Back Scattered Electron (BSE) detectors, located inside the electron column. Images of the TNTA cross-sections were acquired by the in-build STEM detector, on a TEM lamella extracted from the sample surface (lamella was thinned down to less than 30 nm [28]). The layer that can be seen on the top of the nanotubes in the cross-sections is part of the lamella preparation process. It is a Pt protective layer deposited using in turn both the electronic and the ionic beams. EDX maps on the cross-sections were acquired by using the instrument EDAX HI-OCTANE detector.

2.6. XRD characterisation

X-ray powder diffraction (PXRD) scans were acquired at room temperature with a PANalytical X'PERT PRO diffractometer, employing CuKα radiation (λ=1.54187 Å) and a PW3088/60-graded multilayer parabolic X-ray mirror for Cu radiation. The diffractograms were acquired in the 2θ range from 22.0 to 88, using a continuous scan mode with an acquisition step size of 2θ= 0.02638 and a counting time of 49.5 s. QualX2 software and the COD database were used to qualitatively assign the peaks to the structures.

2.7. XPS characterization

AR-XPS experiments were carried out in an UHV chamber with a base pressure lower than 10^{-10} mbar. The chamber was equipped with non-monochromatized Mg (hv=1253.6 eV) and Al (hv=1486.6 eV) radiations and with a hemispherical electron/ion energy analyser (VSW mounting a 16-channel detector). The operating power of the X-ray source was 144 W (12 kV and 12 mA). Photoelectrons were collected at the same of the angle θ between the normal to the sample surface and the analyser maintaining as well the angle between the analyser axis and the X-ray source fixed at 54.5°. All the XPS spectra were measured in fixed analyser transmission mode with pass energy of 44 eV. The binding energy (BE) was calibrated setting the C *1s* peak to 284.5 eV.

3. Results and discussion

3.1. Morphology and composition of the materials and relationship to the deposition conditions

The pristine titanium non-woven web consists of square section fibres with 20 µm edges (Figure - a). It is worth mentioning that anodization of the web requires additional care compared to the anodization of a titanium foil. Heavy anodization can result in complete conversion of the Ti fibres into oxides (thickness largely exceeding 1 µm) with a consistent underlying oxide scale. This massive substitution of metallic Ti with oxide could limit electrical conductivity, and increase the brittleness. This latter fact is detrimental to the mechanical properties of the web. In the worse possible case scenario, fracturing due to the manipulation of this brittle material may lead to the loss of the physical integrity of the electrode.

In the first demonstration of the use of 3D TNTA arrays [15–17], we produced nanotube layers with a thickness exceeding 2 µm with large cracks at the edges of the fibres. The electrodes were solid enough to stand the stress for experiments using a 1 cm^2 electrode, but they were too fragile to design a material suitable for potential scale-up. We observed that even a little bending resulted either in the loss of the oxide from the fibres or a fracture in the electrode structure. Moreover, the aspect ratio of the nanotubes exceeds 15, while for close porosities such as the nanotubes a smaller aspect ratio would be more valuable to improve catalyst utilisation by enhanced mass transport. Accordingly, we decided to switch from the use of organic electrolytes to the use of HF water-based electrolytes. These solutions have been demonstrated to provide shorter nanotubes (< 400 nm) on titanium flat surfaces [29]. Hence, we investigated the following set of growth parameters to help identify the best conditions for the formation of TNTAs on the titanium non-woven web:

- HF concentration (0.2 %, 0.5% and 1% wt)
- Anodization potential (15 and 20 V)
- Anodization time (15, 20 and 30 mins.)

We found that independent nanotubes are obtained with 0.5 % HF in water, at room temperature and with an anodization time and voltage respectively of 20 minutes and 20 V. Figure 1 shows the macro- down to micro-scopic differences between the un-treated mesh and the anodized material. The result we obtained is consistent with the literature on titania nanotube growth on bulk titanium. These nanotubes have an average diameter of 72 nm with an average wall thickness of 8 nm. The average length of the tubes is 250 nm, while the thickness of the underlying oxide is about 30 nm (Figure 3). Accordingly, the aspect ratio is 3.5. Based on the crude approximation that assumes that nanotubes are perfect cylinders, we derived a roughness factor of approximatively 600 meaning that each square centimetre of the geometric area of the support exposes a 600 cm^2 of real surface area.

There is no evidence of cracks at the edges of the fibres, as a consequence of the fact that most of the fibre remains metallic in the core even after the anodization process.

The outcome of the anodization process is highly sensitive to the HF concentration; with 0.2 % HF we observed that nanotubes are gown only on a small fraction of the surface while a significant portion is covered with a continuous oxide layer. A similar oxide layer is obtained when the HF concentration is 0.5%, and the anodization potential is 15 V. With high HF concentrations (>1%) we observed extensive corrosion of the fibres. Corrosion was further enhanced at higher potentials and longer anodization times. Figure 2 reports the surface morphology of the TNTA with both low and high Pd loading. The dropcast sample shows a continuous Pd film, with the summit of the tubes almost completely covered with palladium, leading to a significant reduction of the open diameter of the NT tips. For the samples prepared by PVD, small (less than 20 nm) palladium nanoparticles are present. To better clarify the distribution of palladium inside the nanotubes, we performed a cross-section investigation of the TNTA surface. Figure 3 reports the bright and dark field STEM images acquired on a TEM lamella extracted from the surface of the fibres with a focussed ion beam and a nano-manipulator. We observed that in both samples Pd is also present inside the tubes, but is much more present on the surface for the high loading dropcast sample. This is confirmed by the EDX mapping (Figure 4) of the lamella. Moreover, EDX shows that the bulk oxide layer below the nanotubes is thin, less than 30 nm on average. The STEM analysis also shows that the nanotubes are not entirely independent along the cross-section; they are connected by transversal bridges of titanium dioxide.

The pristine Ti nanotubes sample, together with the two samples with the Pd deposits were analysed via XPS. Figure S2a in the XPS survey scan of the TNTA sample shows the presence of Carbon, Titanium, Oxygen and Fluorine. The presence of fluorine comes from the anodization bath, it is not visible in the catalyst-bearing samples due to the washing cycles the TNTA undergoes prior to the deposition. To shed light on the possible presence of Nickel from the nanotube production procedure, we collected spectra on the same sample, producing the excitation with different energies: hν = 1486.6 eV (Figure S2 b, red line) and hν = 1253.6 eV (Figure S2 b green line) generated by Al and Mg X-ray sources, respectively [30]. As is possible to see the red spectrum in Figure S2b is dominated by the presence of fluorine (F*KLL*) Auger electron spectra [31]. For this reason, we collected the spectra with a Mg source (Figure S2b, green line) because the kineticKinetic energy of the Auger electrons does not depend on the excitation energy, so the F*KLL* peaks do not appear in the Mg-generated spectrum leaving the energy region between 850 eV and 890 eV free from fluorine features. Unfortunately measuring with Mg X-ray source, the region is dominated by Ti*LMM* peaks [31], but a small window from 840eV to 860eV is almost free even if

the background is a bit rough. By comparing the spectrum recorded with a NiO spectrum (Figure S2b, blue line) taken from ref [32], it is possible to assume that the Nickel concentration inside this sample is lower than the detection limit of the XPS experiment (<0.5%).

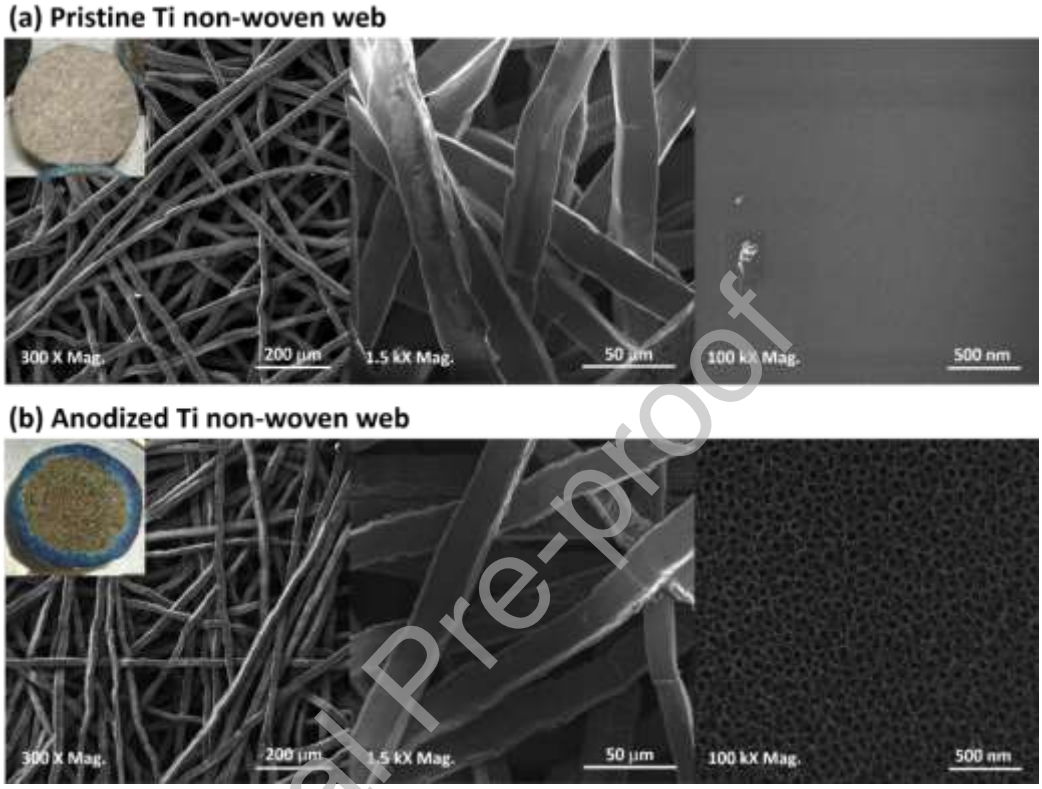

Figure 1 – SEM images of the non-woven web (a) before and (b) after the anodization process (central part of the disk)

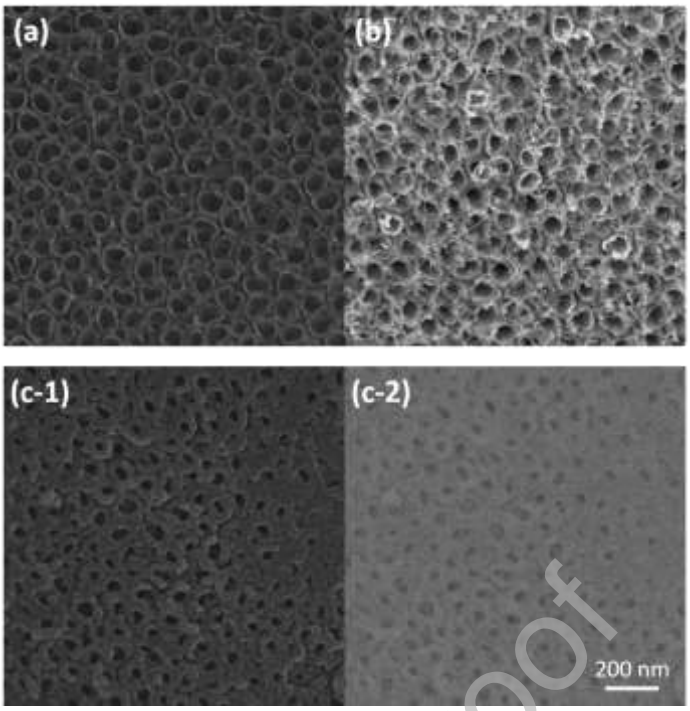

Figure 2 – SEM images of sample surfaces: (a) SEM image of the anodised web, (b) BSE image of the anodised web with a Pd PVD deposit and (c-1 and -2) SE and BSE images of the anodised web with Pd dropcast)

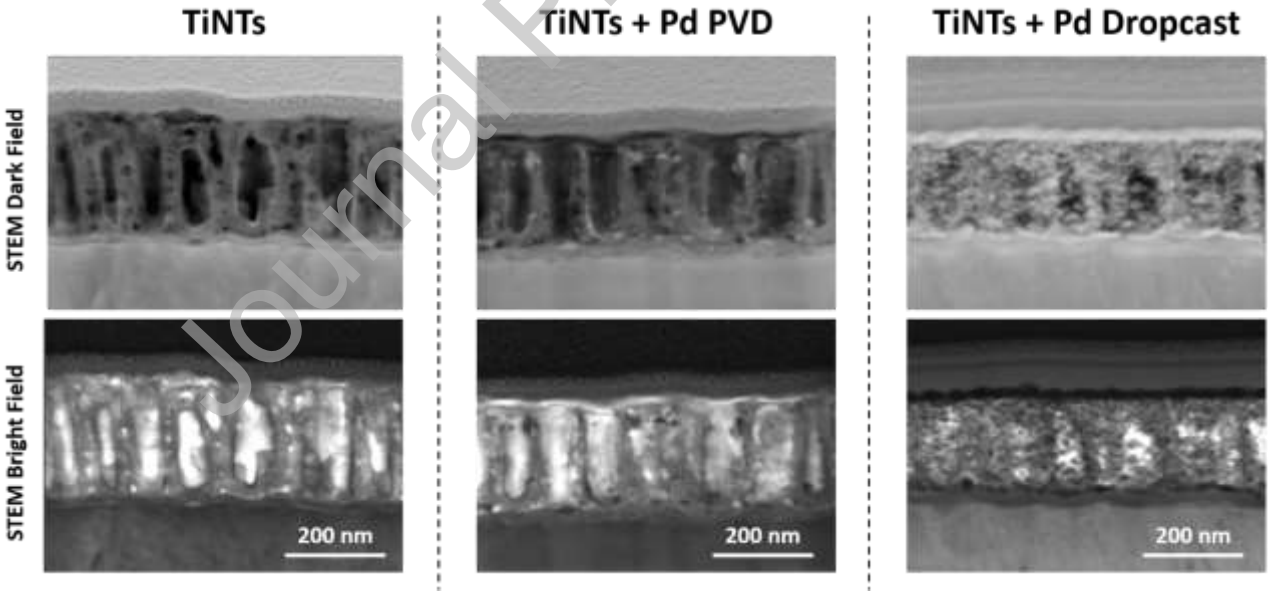

Figure 3 – High magnification STEM images of the TNTA cross sections: Before palladium deposition (left column), after the PVD process (central column) and after dropcast (right column). Images were acquired from TEM lamellas of the surfaces.

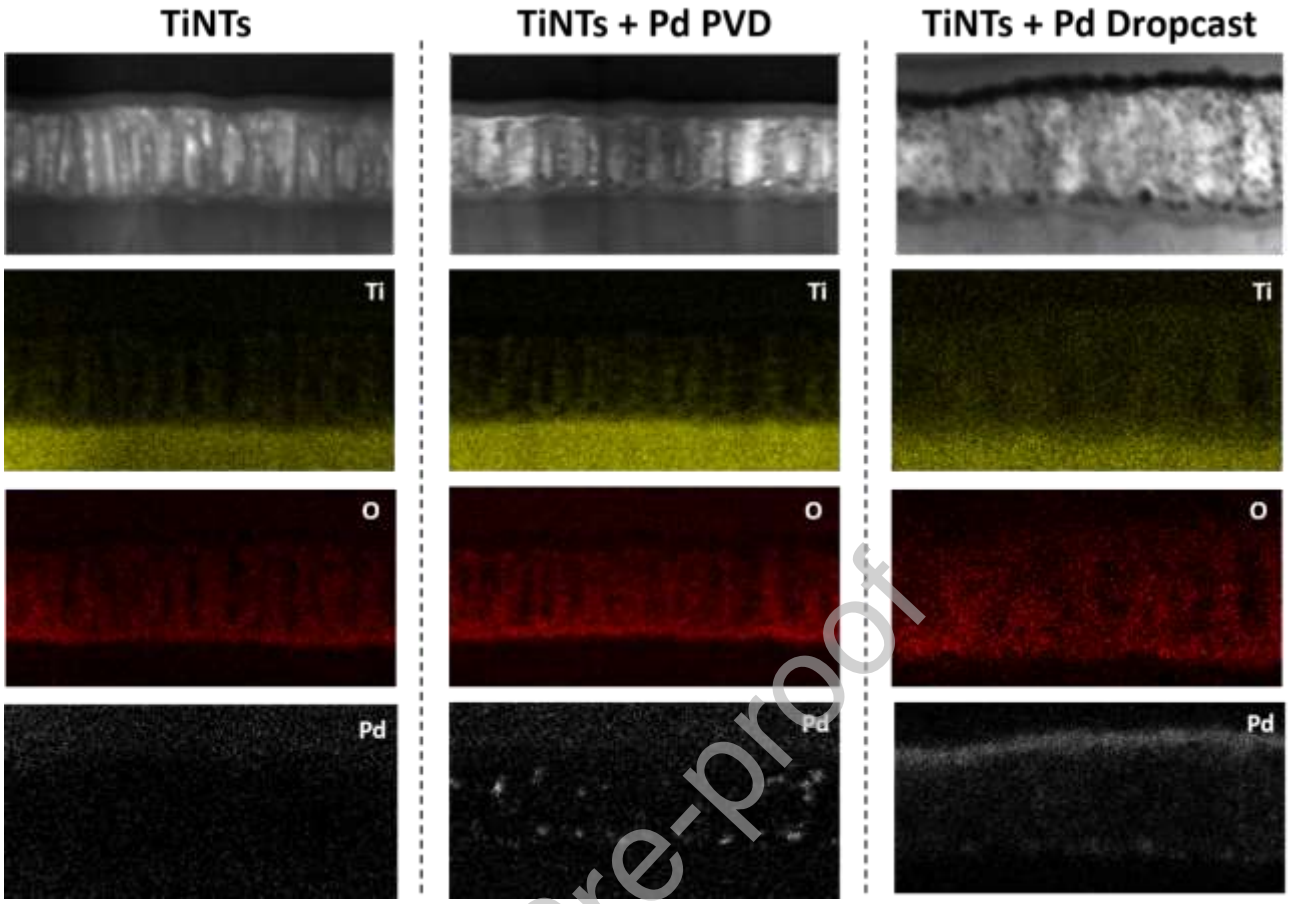

Figure 4 – EDX mapping of the TNTA cross sections of the three series of samples, highlighting Ti and O distribution (yellow and red colour maps, respectively) and Pd presence (grey maps).

3.2. X-ray diffraction

The structural characterisation of the titanium web sample shows that metallic titanium is the main constituent of the fibres (Figure 5). Indeed, all the XRD patterns show the peaks of metallic titanium at 2θ = 35.1 °, 38.2 ° and 40.1 ° that correspond to the maximum intensity reflections (010), (002) and (011). The metallic titanium peaks at 52.9 ° (012), 62.9 ° (110), 70.6 ° (013), 74.1 ° (020), 76.2 ° (112) and 77.3 ° (021) have also been detected. The sample after anodization but without thermal treatment has an XRD pattern similar to metallic Ti, with the exception of the peak at 62.9 ° that is much more intense. The fact that no oxide is detected does not mean that oxide is not present. According to the literature [19] anodization results in the formation of an amorphous nanotube layer with an underlying bulk oxide film. After thermal treatment at 400 °C for 1 h (Figure 5-c) the pattern shows peaks at 25.3° and 47.9°, which are in line with the anatase signals (Figure 5-a), confirming the formation of the oxide that has larger cell parameters compared to metallic titanium [15].

The addition of Pd by dropcast also affects the XRD pattern. In Figure 5 we observe that after Pd dropcasting, the sample shows two low intensity peaks at 2θ = 46.3 ° and 67.6 ° respectively ascribed to the (002) and (113) Pd reflections [15]. The high intensity Pd (111) reflection is partially hidden by the high intensity metallic titanium peaks and is barely detected as a shoulder at the left of the base of the Ti (011) peak. These data indicate that Pd is present in the sample in the metallic state. The sample with Pd PVD does not show any peak related to palladium species. We ascribe this behaviour to the low palladium loading that produces Pd diffraction peaks below the detection limit of the diffractometer.

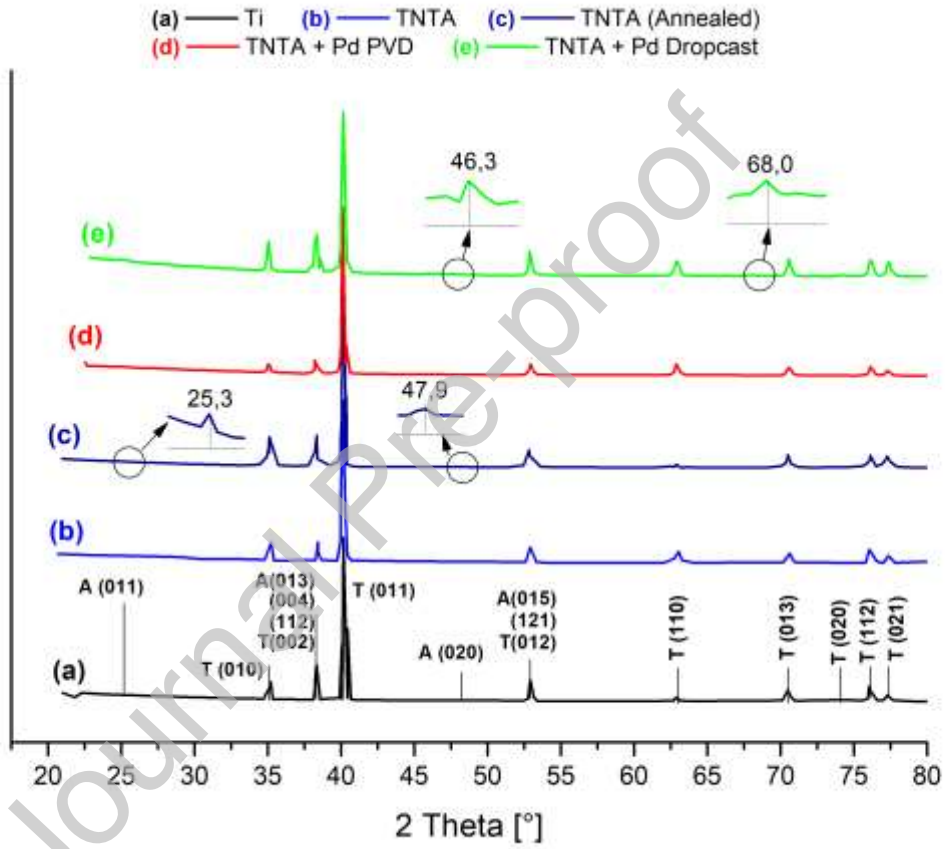

Figure 5 - a comparison of the XRD patterns of (a) the titanium non-woven samples, (b) the non-woven web after anodisation, (c) the non-woven web after anodisation and annealing at 400 °C for 1 h, (d) the non-woven web after anodisation and annealing at 400°C for 1 h + Pd PVD and (e) the non-woven web after anodisation and annealing at 400°C for 1 h + Pd Dropcasting. The Ti pattern (a) is presented together with the most intense Anatase lines, taken from [15] (A for Anatase, T for Metallic Ti)

3.3 Electrochemical characterisation

3.3.1 CV in KOH and $HClO_4$

Figure 6**Error! Reference source not found.**-a reports the cyclic voltammetry in KOH 2M of titanium web, titanium web after anodization and annealing (3D-TNTA) and the 3D TNTA plus the addition of Pd by PVD and dropcast. The CV of the bare Ti web shows a significant anodic current in the whole potential range, with a significant increase in this current above 0.8-0.9 V. We ascribe this current to the oxidation of the Ti electrode. The 3D TNTA sample shows cathodic current at low potentials and a negligible current density above 0.4 V. The lower anodic current compared to the nanotubes results from the fact that the sample is already oxidised and that to proceed further with the oxidation there is the need to provide a large potential to allow further oxides to grow.

The cyclic voltammetry of the 3D TNTA samples with Pd show the typical features of hydrogen absorption and desorption on Pd. Moreover, the unresolved peaks Pa1 and Pa2 (c.a. 0.05V vs RHE), are respectively assigned to current due to the evolution of molecular hydrogen and absorption of hydrogen on Pd (0.25 V RHE, while Pa3 represents hydrogen adsorption on Pd). At potential larger than 0.6-0-7 V we observed a gentle rise in the anodic current related to the formation of Pd oxides. The cathodic current Pc1 and Pc2 (c.a. 0.V vs RHE) is ascribed to the reduction of water and the absorption of hydrogen, while peak Pc3 (c.a. 0.2V vs RHE) is related to Under Potential Deposition (UPD) of hydrogen on Pd. The CV of this sample is in line with what reported in [33]. Peak Pc4 @ 0.65V vs RHE is the result of the reduction of palladium oxides. This peak is extremely important as its associated charge can be used to estimate the Pd surface area. In [34] it is shown that the charge associated to the cathodic peak at 0.65 V corresponds to the formation of the first monolayer of PdO when the upper potential limit is 1.45 V. By integrating peak Pc4 we determined a specific surface area of Pd of 1.61 $m^2\ g^{-1}$ for the low loading catalyst, while we found 0.86 $m^2\ g^{-1}$ for the high loading dropcast catalyst. CVs were also recorded on the same samples in a $HClO_4$ 0.25 M electrolyte (Figure 66-b).

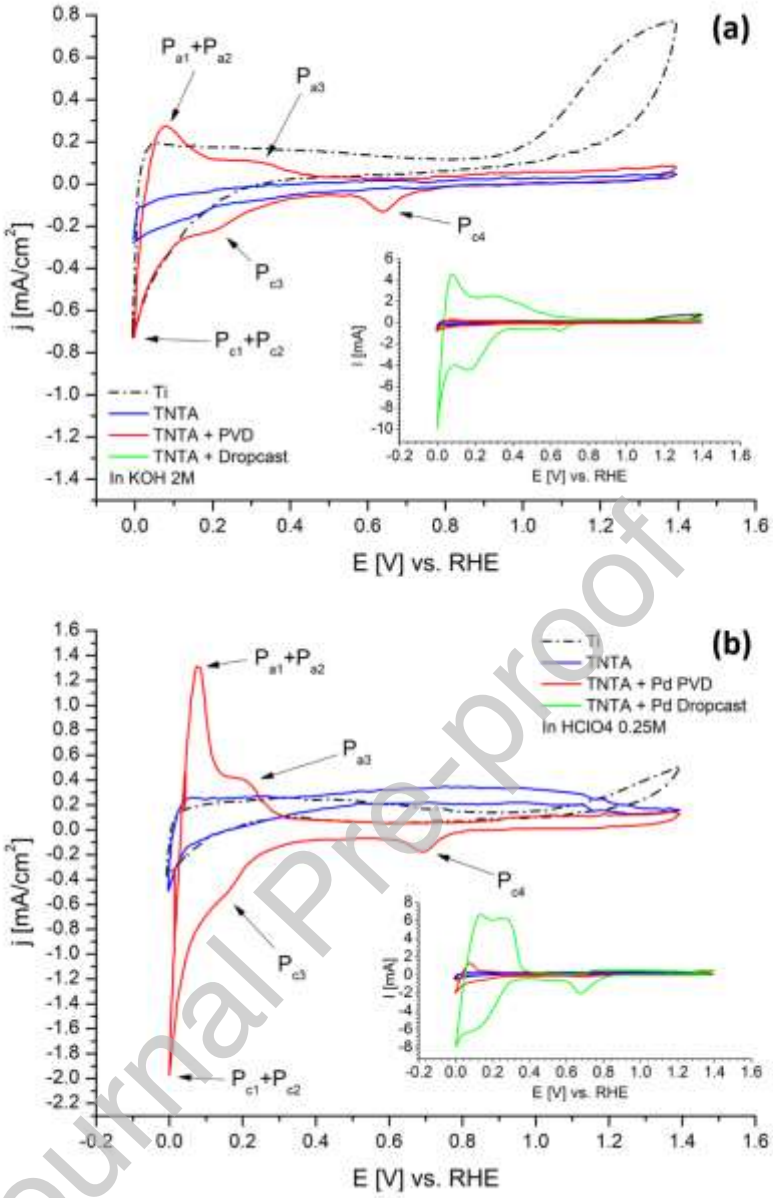

Figure 6 – (a) cyclic voltammetry of the anodised and annealed non-woven web in KOH 2M before and after the addition of Pd by PVD and dropcast. (b) Cyclic voltammetry of the anodised and annealed non-woven web in HClO4 0.25 M before and after the addition of Pd by PVD and dropcast.

Curves of Ti and TNTA in Figure 66-b show the absence of any defined peaks. The CV of the PVD Pd sample shows cathodic peaks Pc1 (c.a. 0V vs RHE), Pc2 (c.a. 0V vs RHE) and Pc3 (c.a. 0.2V vs RHE) that are similar to what observed in alkali, we ascribe to the evolution of molecular hydrogen, absorption and adsorption of hydrogen species on the surface of palladium nanoparticles by underpotential deposition. Accordingly, the anodic scan shows the corresponding anodic peaks Pa1 (c.a. 0.05V vs RHE), Pa2 (c.a. 0.05V vs RHE) and Pa3 (c.a. 0.2V vs RHE) ascribed to the oxidation

of molecular hydrogen, the oxidation of the absorbed hydrogen. [34] Peak Pc4 (c.a. 0.7V vs RHE) is again related to the reduction of the Palladium oxides (II) PdO that form on the surface of the nanoparticle in direct scanning to potentials higher than 0.6V vs RHE [34].

3.3.2 Catalyst functionality: activity toward HER, OER and test in an alkaline membrane water electrolyser

To explore the activity of the catalysts for HER and OER in both alkaline and acidic conditions, we performed slow-scan Linear Sweep Voltammetry (LSV) in the pertinent potential range (Figure 7).
Figure 7-a shows that the catalytic activity in terms of maximum current density at -0.4 V vs RHE for HER in alkaline conditions increases in the sense TNTA < Ti < Pd PVD < Pd Dropcast< Pt: -10.8 mA cm^{-2} < -12.2 < -18.7 <-102 < -148.1 mA cm^{-2}. Not surprisingly titanium oxide does not show a significant activity toward the hydrogen evolution reaction. The addition of Pd to the 3D-TNTA provides an 80% increase of the current compared to the TNTA. However, this performance does not compete with that of the Pt-based catalyst that is 3 times higher than that of the Pd catalyst. The resulting specific activity of Pd @ -0.4 V was -264.1 mA/mg.
Figure 7-b shows that in $HClO_4$ 0.25 M the activity for HER of the samples follows the order: in Ti < TNTA < Pd TNTA < Pt: -17.5 < -21.5 < -31.0 < -47.0 < -54.0 mA cm^{-2}. The activity in acidic environment resulted higher than in alkaline conditions leading to a mass-specific current density of the low loading Pd catalyst of -440 mA/mg. The LSVs of the high loading sample show the presence of a peak prior to hydrogen evolution. This peak is more evident for the HER in $HClO_4$ than in KOH where it is barely visible. We ascribe this to hydrogen adsorption, analogous to what we observed in the cyclic voltammetries (P_{c3} shoulders) already discussed in the previous section and reported in fig. 6. The fact that the peak is more resolved in fig 7 than in fig. 6 depends on the different scan rate (1 mV s^{-1} vs. 20 mV s^{-1}). However, we do not recommend the use of these catalysts in strongly acidic environments. Indeed, in these conditions, Ti-based materials can undergo cathodic corrosion according to the Pourbaix diagram of Ti. Even in acid, Pt/C catalyst is the most performing, however we may hypothesise that an ultra-low Pd catalyst engineered to achieve a large surface area could improve this activity. Metallic Pd is stable in the potential range of experienced by a cathode in an electrolyser [35].
The Oxygen Evolution Performance in KOH 2M was investigated by LSV on KOH 2M, and is reported in Figure 7-c. In this case we show that the current density @2.2 V for the Pd PVD sample is almost the same 6.6 mA cm^{-2} of that of the pristine TNTA providing no significant advantages in adding such a limited amount of Pd to improve the catalytic activity. The TNTA shows a current density @ 2.2 V 20% larger than the pristine titanium non-woven web support. The high loading Pd

dropcast electrocatalyst showed a current density of 87 mA cm^{-2} @ 2.2 V with a 13-fold improvement compared to the bare TNTA. The IrO_2 reference sample delivered 220 mA cm^{-2} @ 2.2 being the most performing catalyst. However, it is worth mentioning that the use of Pd under strongly anodic conditions in alkali is not recommended. The Pd Pourbaix diagram indeed shows that Pd can be lost through dissolution forming hydroxypalladate species [35–37].

We also tested the activity toward the oxygen evolution reaction in acidic electrolytes (Figure 7-d), recording current densities significantly lower compared to alkaline electrolytes. We observed that @ 2.2 V the low-loading PVD Pd electrocatalyst provides a limited advantage over the TNTA, delivering 6.2 mA cm^{-2} against the 4.5 of the TNTA. The high loading Pd delivered 53.5 mA $cm^{-2,}$ with a specific activity of 31.4 mA cm^{-2}. The activity of the low loading PVD sample was 86.6 mA/mg. A comparison of these two values shows that the increase of the activity in the PVD is greater than what expected from considering the specific surface area of the two, indicating a larger activity per unit area of the latter. One possible explanation for this phenomenon might by the presence of porosities in the dropcast sample that may be obstructed by the formation of hard-to-remove gas bubbles. Stability concerns on the use of Pd at anodic potentials in acid exists. The Pourbaix diagram of Pd shows that Pd can dissolve as aqueous Pd^{2+} in acids, a fact that may severely hamper the stability. On the basis of the activity and stability considerations given above, both for titanium and palladium we conclude that the catalyst we propose must operate in cathodic condition and in alkali to guarantee stability. For this reason, we decided to test these samples as cathodes in an alkaline membrane electrolyser.

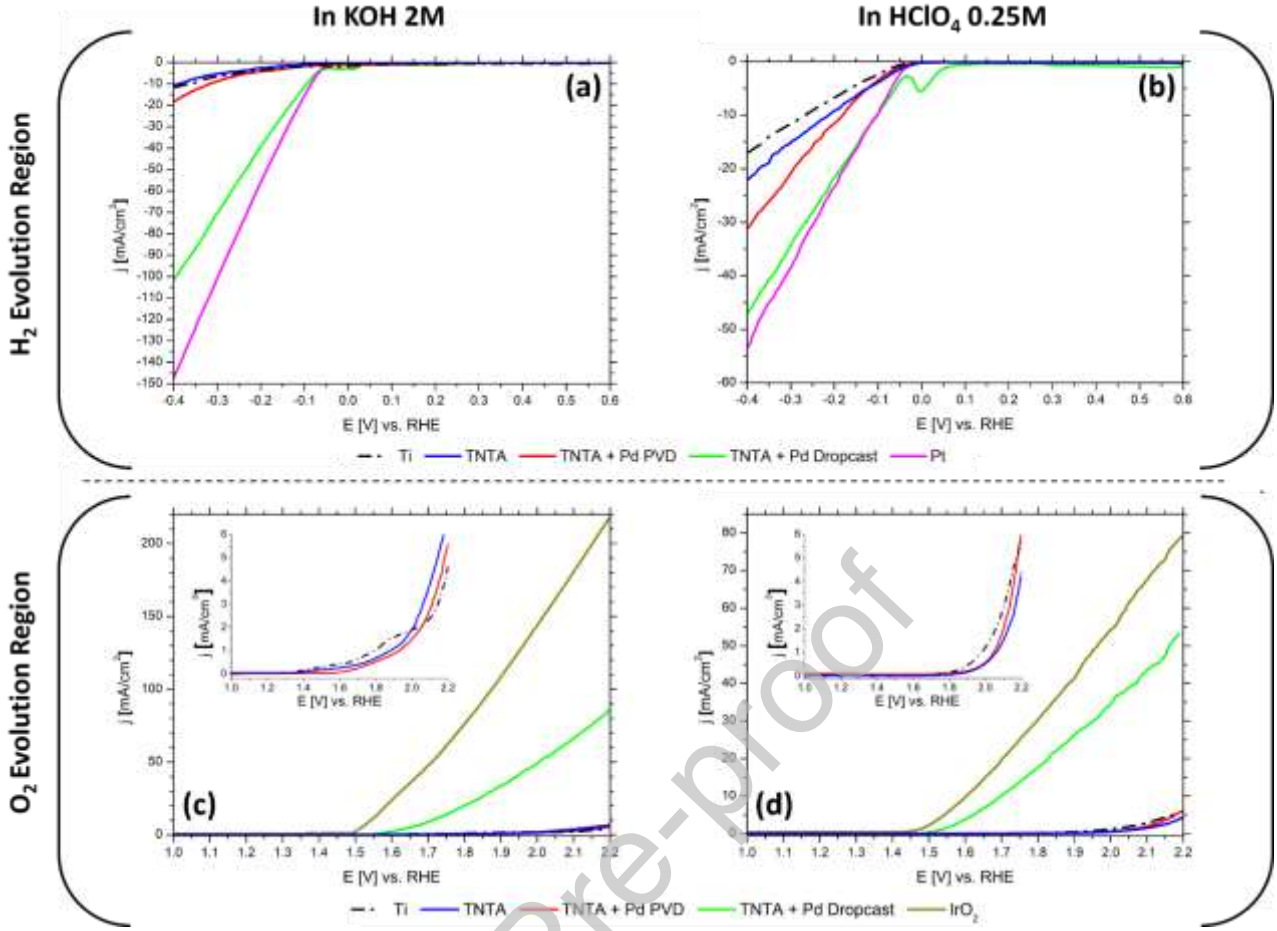

Figure 7 - LSV of the hydrogen evolution region in KOH 2M (a) and HClO4 0.25M (b); LSV of the oxygen evolution region in KOH 2M (c) and HClO4 0.25M (d)

Table 1 - Overview of the AEM electrolyser performance

T_{cell}= 60°C	J (mA cm^{-2}) @2.5V	E_{onset} (V)
Dropcast	1800	1.76
PVD	1485	1.76
TNTA	634	1.87
Ti	412	1.87
Pt	1849	1.52

Figure 8 reports the result of the testing of the 3D TNTA based materials as cathode in an alkaline water electrolyser operating with KOH 2M electrolyte @ 60 °C. To show the effectiveness of the catalyst, we first performed experiments with the bare non-woven titanium web and the same sample after anodization. We observed that these samples show the same onset potential at 1.87 V. However, the sample with the titania nanotubes showed a better performance @ 2.5 V delivering

634 mA against the 412 mA of the new non-woven web (Table 1). Performance is better with the addition of Pd. With the low loading PVD sample, the onset potential decreases to 1.76 V. At 2 V; the electrolyser delivers a current density of 280 mA cm^{-2}. At 2.5 V the current density for the PVD sample is 1485 mA cm^{-2}. This is a remarkable result that shows that this cathode architecture can produce high current densities. The system equipped with platinum delivered 1849 mA cm^{-2} @ 2.5 V and 750 mA cm^{-2} @ 2 V that is only slightly better than the performance of the high loading Pd dropcast catalyst (1800 mA cm^{-2} @ 2.5 V and 690 mA cm^{-2} @ 2 V). Remarkably, the current density delivered by the PVD sample did not change significantly after 24 hours of galvanostatic operation at 1 A cm^{-2} (Figure S3). A SEM inspection after the operation did not show significant alteration of the surface morphology of the samples (Figure 9)

We believe that much of the origin of the relatively low performance of the Pd electrodes resides in the lower specific surface area of the Pd catalysts compared to the real surface area of Pt/C and IrO_2 catalysts. Indeed, recent literature has reported that Pt/C has a surface area of 41 m^2/g. Considering that the Pt/C catalyst has 0.4 mg cm^{-2} [38] the Pt specific surface area in the electrode is 160 cm^2. A simple calculation based on the loading of the Pd catalysts and the respective surface areas indicates that the sample deposited by PVD has a surface area of 0.7 cm^2, while the dropcast sample achieves 27 cm^2. Accordingly, in Table 2 a comparison of the performance of the materials normalised for the metal specific surface area of the catalysts is shown. It is worth mentioning that to calculate the activity of the PVD sample, we have considered a current density value corresponding to the difference between the current density of Pd samples minus the current density of the TNTA. This hypothesis is conservative, and we applied it to not overestimate the normalised activity by including the contribution of the activity of the TNTA. These data show that the palladium samples show a real surface area normalized activity larger than Pt (table 2)

Table 2 – Current density values extracted for the Pd PVD and Pd Dropcast samples from HER LSV in KOH 2M: J_{ga} related to the geometric area, J_m to catalyst mass and J_{ra} to the real exposed surface of the TNTA. Current density values for Pd deposits are calculated by subtracting the current density value of the bare TNTA.

	J_{ga} [mA/cm^2] @ -0.2 V	**J_m [mA/mg] @ -0.2 V**	**J_{ra} [mA/cm^2] @ -0.2 V**
TNTA + Pd PVD	-1.83	-22.59	-1.40
TNTA + Pd Dropcast	-35.6	-20.94	-2.43
Pt/C	-54.8	-137.00	-0.31

The high specific activity, indicates that the enginerization of the catalyst to increase the roughness factor would boost the performance. Unfortunately, most of the known methods to obtain palladium nanoparticles onto carbon-based support cannot be exported to this new class of substrate. Indeed, the classical deposition methods based on the suspension of the support in the solution where palladium salt is reduced cannot be applied. The optimisation of the performance will require an effort in the development of deposition methods (e.g. dropcasting, electrodeposition, vapour phase methods) to provide small nanoparticles and ultimately to have catalysts with enhanced catalyst mass activity, but this is a definitely an achievable target.

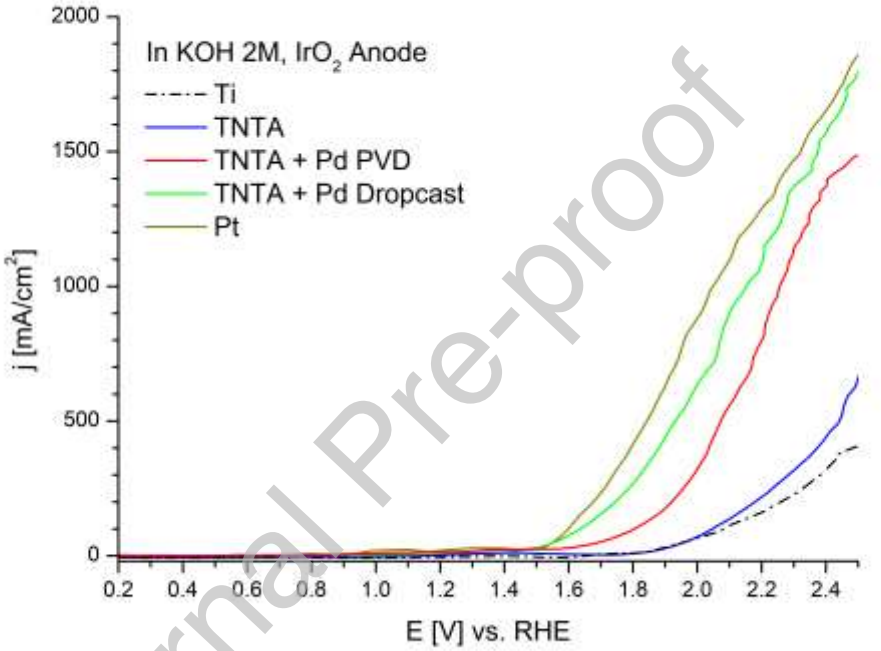

Figure 8 - Performance of an electrolyser equipped with a IrO_2 anode and TNTA cathodes: potentiodynamic curve.

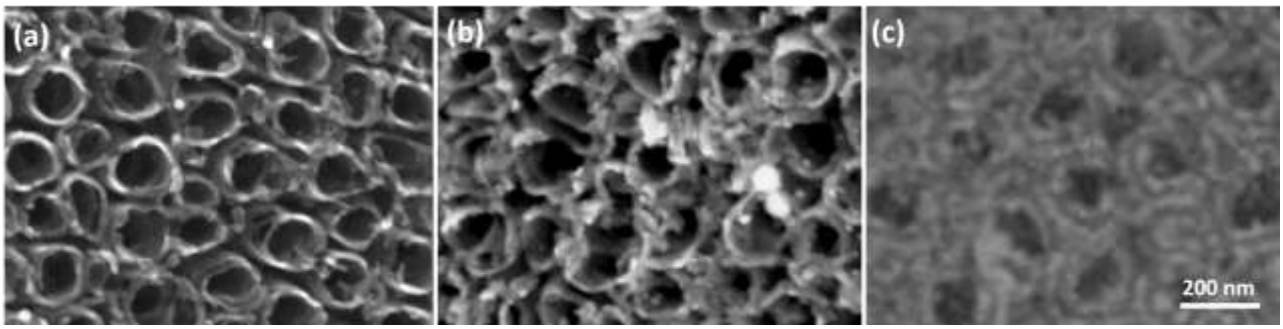

Figure 9 - SEM characterisation of (a) the TNTA, (b) the PVD Pd TNTA and (c) Dropcast Pd TNTA after 24 h of electrolysis operations at 1A cm^{-2}

4. Conclusions

We have developed and optimized the synthesis of short and low aspect ratio titania nanotube arrays on a commercial titanium non-woven web. The best conditions: 1) HF 0.5 % wt. in water; 2) anodization time 20 min. and 3) anodization voltage 20 V, produce a uniform layer (250 nm tall, 72 nm wide) of nanotubes with a small (30 nm) oxide layer separating the NTs from the bulk titanium metal fibres. This robust electrode support was treated with Pd by two methods; ultralow Pd loading (with PVD – 81 µg cm^{-2}) and high Pd loading (by dropcast 1.7 mg cm^{-2}). The specific Pd electrochemically active surfaces determined by CV of the PVD and dropcast samples were 1.61 m^2 g^{-1} and 0.86 m^2 g^{-1} respectively. All samples were tested in electrochemical cells (CV, LSV) to determine the catalytic activity towards both the hydrogen and oxygen evolution reactions, both in acid ($HClO_4$ 0.25M) and alkali (KOH 2M). The HOR and OER activities were benchmarked with Pt/C and IrO_2 catalysts respectively. We found that the ultralow Pd loaded sample (PVD) exhibits a significant improvement in the HER activity in alkaline media with the Pd area specific activity significantly greater than Pt/C. All of the TNTA based samples were applied as cathodes in a complete AEM water electrolysis cell. The tests show that the AEM electrolyser with the low loading PVD cathode delivers 280 mA cm^{-2} @ 2V. and 1485 mA cm^{-2} @ 2.5V. Although this performance is less than the benchmark Pt/C cathode, it is quite remarkable considering the 5 x lower metal loading. We believe that this new class of HER catalyst has the potential to operate at very high current densities with an ultralow Pd loading after further optimisation of the Pd specific surface. This will be achieved through electrochemical post- processing [39]. On the basis of the findings reported in this paper, we conclude that the use of ultralow Pd loading electrocatalysts supported on short and low-aspect ratio titania nanotubes has a concrete potential as an efficient cathode for alkaline membrane water electrolysis.

Funding:

"Fondazione CR Firenze" through projects: "Richiesta contributo per acquisto di un microscopio elettronico a scansione ad ultra-alta risoluzione per potenziare il Centro di Microscopie Elettroniche (Ce.M.E.) and "EnergyLab"; POR FESR 2014-2020 project FELIX (Fotonica ed Elettronica Integrate per l'Industria), project code n. 6455; PRIN 2017 project funded by the Italian Ministry for University and Research (MUR) (grant n. 2017YH9MRK). The authors also thank the Italian ministry MUR for funding through the FISR 2019 project AMPERE (FISR2019_01294).

Credit Author Statement:

M. Bellini: Methodology, Investigation, Writing - Original Draft, Writing - Review & Editing **E. Berretti:** Investigation, Writing - Original Draft, Writing - Review & Editing, Visualization **M. Innocenti**: Supervision **G. Magherini:** Investigation, Visualization **M. V. Pagliaro:** Investigation **L.Poggini.:** Investigation **H. A. Miller:** Methodology**,** Validation, Investigation, Writing - Original Draft, Writing - Review & Editing

A. Lavacchi: Conceptualization, Methodology, Validation, Writing - Original Draft, Writing - Review & Editing **F. Vizza:** Resources, Supervision

Declaration of interests

The authors declare that they have no known competing financial interests or personal relationships that could have appeared to influence the work reported in this paper.

References:

[1] K. Ayers, N. Danilovic, R. Ouimet, M. Carmo, B. Pivovar, M. Bornstein, Perspectives on Low-Temperature Electrolysis and Potential for Renewable Hydrogen at Scale, Annu. Rev. Chem. Biomol. Eng. 10 (2019) 219–239. https://doi.org/10.1146/annurev-chembioeng-060718-030241.

[2] K. Ayers, The potential of proton exchange membrane–based electrolysis technology, Curr. Opin. Electrochem. 18 (2019) 9–15. https://doi.org/10.1016/j.coelec.2019.08.008.

[3] N. Danilovic, K.E. Ayers, C. Capuano, J.N. Renner, L. Wiles, M. Pertoso, (Plenary) Challenges in Going from Laboratory to Megawatt Scale PEM Electrolysis, ECS Trans. 75 (2016) 395–402. https://doi.org/10.1149/07514.0395ecst.

[4] J. Brauns, T. Turek, Alkaline Water Electrolysis Powered by Renewable Energy: A Review, Processes. 8 (2020) 248. https://doi.org/10.3390/pr8020248.

[5] H.A. Miller, K. Bouzek, J. Hnat, S. Loos, C.I. Bernäcker, T. Weißgärber, L. Röntzsch, J. Meier-Haack, Green hydrogen from anion exchange membrane water electrolysis: a review of recent developments in critical materials and operating conditions, Sustain. Energy Fuels. 4 (2020) 2114–2133. https://doi.org/10.1039/C9SE01240K.

[6] I. Vincent, D. Bessarabov, Low cost hydrogen production by anion exchange membrane electrolysis: A review, Renew. Sustain. Energy Rev. 81 (2018) 1690–1704. https://doi.org/10.1016/j.rser.2017.05.258.

[7] A.K. Niaz, A. Akhtar, J.-Y. Park, H.-T. Lim, Effects of the operation mode on the degradation behavior of anion exchange membrane water electrolyzers, J. Power Sources. 481 (2021) 229093. https://doi.org/10.1016/j.jpowsour.2020.229093.

[8] X. Yan, X. Yang, X. Su, L. Gao, J. Zhao, L. Hu, M. Di, T. Li, X. Ruan, G. He, Twisted ether-free polymer based alkaline membrane for high-performance water electrolysis, J. Power Sources. 480 (2020) 228805. https://doi.org/10.1016/j.jpowsour.2020.228805.

[9] F. Safizadeh, E. Ghali, G. Houlachi, Electrocatalysis developments for hydrogen evolution reaction in alkaline solutions – A Review, Int. J. Hydrogen Energy. 40 (2015) 256–274. https://doi.org/10.1016/j.ijhydene.2014.10.109.

[10] N.-T. Suen, S.-F. Hung, Q. Quan, N. Zhang, Y.-J. Xu, H.M. Chen, Electrocatalysis for the oxygen evolution reaction: recent development and future perspectives, Chem. Soc. Rev. 46 (2017) 337–365. https://doi.org/10.1039/C6CS00328A.

[11] C. Rozain, E. Mayousse, N. Guillet, P. Millet, Influence of iridium oxide loadings on the performance of PEM water electrolysis cells: Part I–Pure IrO 2 -based anodes, Appl. Catal. B Environ. 182 (2016) 153–160. https://doi.org/10.1016/j.apcatb.2015.09.013.

[12] C. Rozain, E. Mayousse, N. Guillet, P. Millet, Influence of iridium oxide loadings on the performance of PEM water electrolysis cells: Part II – Advanced oxygen electrodes, Appl. Catal. B Environ. 182 (2016) 123–131. https://doi.org/10.1016/j.apcatb.2015.09.011.

[13] A. Lim, J. Kim, H.J. Lee, H.-J. Kim, S.J. Yoo, J.H. Jang, H. Young Park, Y.-E. Sung, H.S. Park, Low-loading IrO2 supported on Pt for catalysis of PEM water electrolysis and regenerative fuel cells, Appl. Catal. B Environ. 272 (2020) 118955. https://doi.org/10.1016/j.apcatb.2020.118955.

[14] M. Keersemaker, Critical Raw Materials, (2020) 69–82. https://doi.org/10.1007/978-3-030-40268-6_9.

[15] Y.X. Chen, A. Lavacchi, H.A. Miller, M. Bevilacqua, J. Filippi, M. Innocenti, A. Marchionni, W. Oberhauser, L. Wang, F. Vizza, Nanotechnology makes biomass electrolysis more energy efficient than water electrolysis, Nat. Commun. 5 (2014) 4036. https://doi.org/10.1038/ncomms5036.

[16] Y. Chen, M. Bellini, M. Bevilacqua, P. Fornasiero, A. Lavacchi, H.A. Miller, L. Wang, F. Vizza, Direct Alcohol Fuel Cells: Toward the Power Densities of Hydrogen-Fed Proton Exchange Membrane Fuel Cells, ChemSusChem. 8 (2015) 524–533.

https://doi.org/10.1002/cssc.201402999.

[17] H.A. Miller, A. Lavacchi, F. Vizza, Storage of renewable energy in fuels and chemicals through electrochemical reforming of bioalcohols, Curr. Opin. Electrochem. 21 (2020) 140–145. https://doi.org/10.1016/j.coelec.2020.02.001.

[18] Y.X. Chen, V. Gombac, T. Montini, A. Lavacchi, J. Filippi, H.A. Miller, P. Fornasiero, F. Vizza, An increase in hydrogen production from light and ethanol using a dual scale porosity photocatalyst, Green Chem. 20 (2018) 2299–2307. https://doi.org/10.1039/C7GC03508J.

[19] P. Roy, S. Berger, P. Schmuki, TiO2 Nanotubes: Synthesis and Applications, Angew. Chemie Int. Ed. 50 (2011) 2904–2939. https://doi.org/10.1002/anie.201001374.

[20] G.K. Mor, O.K. Varghese, M. Paulose, K. Shankar, C.A. Grimes, A review on highly ordered, vertically oriented TiO2 nanotube arrays: Fabrication, material properties, and solar energy applications, Sol. Energy Mater. Sol. Cells. 90 (2006) 2011–2075. https://doi.org/10.1016/j.solmat.2006.04.007.

[21] C. Xu, J. Yang, E. Liu, Q. Jia, G.M. Veith, G. Nair, S. DiPietro, K. Sun, J. Chen, P. Pietrasz, Z. Lu, M. Jagner, K.K. Gath, S. Mukerjee, J.R. Waldecker, Physical vapor deposition process for engineering Pt based oxygen reduction reaction catalysts on NbOx templated carbon support, J. Power Sources. 451 (2020) 227709. https://doi.org/10.1016/j.jpowsour.2020.227709.

[22] S. Liu, X. Mu, H. Duan, C. Chen, H. Zhang, Pd Nanoparticle Assemblies as Efficient Catalysts for the Hydrogen Evolution and Oxygen Reduction Reactions, Eur. J. Inorg. Chem. 2017 (2017) 535–539. https://doi.org/10.1002/ejic.201601277.

[23] L. Zhang, Q. Chang, H. Chen, M. Shao, Recent advances in palladium-based electrocatalysts for fuel cell reactions and hydrogen evolution reaction, Nano Energy. 29 (2016) 198–219. https://doi.org/10.1016/j.nanoen.2016.02.044.

[24] S. Sarkar, S.C. Peter, An overview on Pd-based electrocatalysts for the hydrogen evolution reaction, Inorg. Chem. Front. 5 (2018) 2060–2080. https://doi.org/10.1039/C8QI00042E.

[25] A. Barhoum, H.H. El-Maghrabi, I. Iatsunskyi, E. Coy, A. Renard, C. Salameh, M. Weber, S. Sayegh, A.A. Nada, S. Roualdes, M. Bechelany, Atomic layer deposition of Pd nanoparticles on self-supported carbon-Ni/NiO-Pd nanofiber electrodes for electrochemical hydrogen and oxygen evolution reactions, J. Colloid Interface Sci. 569 (2020) 286–297. https://doi.org/10.1016/j.jcis.2020.02.063.

[26] M. Ge, J. Cai, J. Iocozzia, C. Cao, J. Huang, X. Zhang, J. Shen, S. Wang, S. Zhang, K.-Q. Zhang, Y. Lai, Z. Lin, A review of TiO 2 nanostructured catalysts for sustainable H 2 generation, Int. J. Hydrogen Energy. 42 (2017) 8418–8449. https://doi.org/10.1016/j.ijhydene.2016.12.052.

[27] X. Chen, S.S. Mao, Titanium Dioxide Nanomaterials: Synthesis, Properties, Modifications, and Applications, Chem. Rev. 107 (2007) 2891–2959. https://doi.org/10.1021/cr0500535.

[28] W. Giurlani, E. Berretti, M. Innocenti, A. Lavacchi, Measuring the Thickness of Metal Coatings: A Review of the Methods, Coatings. 10 (2020) 1211. https://doi.org/10.3390/coatings10121211.

[29] J. Bai, B. Zhou, L. Li, Y. Liu, Q. Zheng, J. Shao, X. Zhu, W. Cai, J. Liao, L. Zou, The formation mechanism of titania nanotube arrays in hydrofluoric acid electrolyte, J. Mater. Sci. 43 (2008) 1880–1884. https://doi.org/10.1007/s10853-007-2418-8.

[30] O. Bondarchuk, A.P. LaGrow, A. Kvasha, T. Thieu, E. Ayerbe, I. Urdampilleta, On the X-ray photoelectron spectroscopy analysis of LiNixMnyCozO2 material and electrodes, Appl. Surf. Sci. 535 (2021) 147699. https://doi.org/10.1016/j.apsusc.2020.147699.

[31] P.E.S. and K.D.B. J. F. Moulder, W. F. Stickle, Handbook of X-ray photoelectron spectroscopy: a reference book of standard spectra for identification and interpretation of XPS data, Perkin-Elmer Corporation, Eden Prairie, Minnesota, USA, 1992.

[32] M.C. Biesinger, L.W.M. Lau, A.R. Gerson, R.S.C. Smart, The role of the Auger parameter in XPS studies of nickel metal, halides and oxides, Phys. Chem. Chem. Phys. 14 (2012) 2434. https://doi.org/10.1039/c2cp22419d.

[33] B.F. Machado, A. Marchionni, R.R. Bacsa, M. Bellini, J. Beausoleil, W. Oberhauser, F. Vizza, P. Serp, Synergistic effect between few layer graphene and carbon nanotube supports for palladium catalyzing electrochemical oxidation of alcohols, J. Energy Chem. 22 (2013) 296–304. https://doi.org/10.1016/S2095-4956(13)60036-4.

[34] M. Grdeń, M. Łukaszewski, G. Jerkiewicz, A. Czerwiński, Electrochemical behaviour of palladium electrode: Oxidation, electrodissolution and ionic adsorption, Electrochim. Acta. 53 (2008) 7583–7598. https://doi.org/10.1016/j.electacta.2008.05.046.

[35] G. Montegrossi, A. Giaccherini, E. Berretti, F. Di Benedetto, M. Innocenti, F. D'Acapito, A. Lavacchi, Computational Speciation Models: A Tool for the Interpretation of Spectroelectrochemistry for Catalytic Layers under Operative Conditions, J. Electrochem.

Soc. 164 (2017) E3690–E3695. https://doi.org/10.1149/2.0711711jes.

[36] L. Wang, A. Lavacchi, M. Bellini, F. D'Acapito, F. Di Benedetto, M. Innocenti, H.A. Miller, G. Montegrossi, C. Zafferoni, F. Vizza, Deactivation of Palladium Electrocatalysts for Alcohols Oxidation in Basic Electrolytes, Electrochim. Acta. (2015). https://doi.org/10.1016/j.electacta.2015.02.026.

[37] Berretti, Giaccherini, Montegrossi, D'Acapito, Di Benedetto, Zafferoni, Puri, Lepore, Miller, Giurlani, Innocenti, Vizza, Lavacchi, In-situ Quantification of Nanoparticles Oxidation: A Fixed Energy X-ray Absorption Approach, Catalysts. 9 (2019) 659. https://doi.org/10.3390/catal9080659.

[38] P.G. Corradini, F.I. Pires, V.A. Paganin, J. Perez, E. Antolini, Effect of the relationship between particle size, inter-particle distance, and metal loading of carbon supported fuel cell catalysts on their catalytic activity, J. Nanoparticle Res. 14 (2012) 1080. https://doi.org/10.1007/s11051-012-1080-5.

[39] Y.-X. Chen, A. Lavacchi, S.-P. Chen, F. di Benedetto, M. Bevilacqua, C. Bianchini, P. Fornasiero, M. Innocenti, M. Marelli, W. Oberhauser, S.-G. Sun, F. Vizza, Electrochemical Milling and Faceting: Size Reduction and Catalytic Activation of Palladium Nanoparticles, Angew. Chemie Int. Ed. 51 (2012) 8500–8504. https://doi.org/10.1002/anie.201203589.